Nanoscale

PAPER

View Article Online
View Journal | View Issue

Cite this: *Nanoscale*, 2024, **16**, 11575

Hydrodeoxygenation of anisole over SBA-15-supported Ni, Pd, and Pt mono- and bimetallic catalysts: effect of the metal's nature on catalytic activity and selectivity†

Daniel E. Pérez-Estrada, [a] Haydee Vargas-Villagrán,[a] Rubén Mendoza-Cruz [b] and Tatiana E. Klimova *[a]

Monometallic Ni, Pd and Pt and bimetallic catalysts formed by combinations of the above metals supported on SBA-15 silica were synthesized, characterized and tested in the hydrodeoxygenation reaction of anisole. The objective of the work was to detect the effect of the nature of metals on the activity of the catalysts at different steps of anisole hydrodeoxygenation: hydrogenation of the aromatic ring of anisole and C–O bond cleavage in the intermediate cyclohexyl methyl ether. The support and the catalysts were characterized by N_2 physisorption, X-ray diffraction, UV-vis diffuse reflectance spectroscopy, temperature-programmed reduction, scanning electron microscopy-energy dispersive X-ray spectroscopy, transmission electron microscopy and HAADF-STEM. The catalytic activity tests were carried out in a batch reactor at 280 °C and 7.3 MPa pressure. The activity results show that the NiPd/SBA-15 catalyst had the greatest ability for hydrogenation of the aromatic ring of anisole, while its NiPt/SBA-15 analog resulted in better activity for C–O bond hydrogenolysis. The bimetallic NiPt/SBA-15 catalyst showed the best catalytic performance in the HDO of anisole ascribed to the formation of a Ni–Pt alloy. On the other hand, the combination of Pd and Pt metals in the PdPt/SBA-15 catalyst resulted in the formation of bimetallic particles with Pd-rich and Pt-rich domains, showing high selectivity for the formation of the cyclohexyl methyl ether, which can be useful for the hydrogenation of aromatic rings in O-containing reactants with the formation of saturated O-containing products. According to the characterization results (HAADF-STEM), the different catalytic behavior of NiPd/SBA-15, NiPt/SBA-15, and PdPt/SBA-15 catalysts could be attributed to different characteristics of the bimetallic active phases in them.

Received 19th March 2024,
Accepted 22nd May 2024

DOI: 10.1039/d4nr01222d

rsc.li/nanoscale

1. Introduction

Global greenhouse gas emissions continue increasing every year. In 2022, greenhouse gas (GHG) emissions have set a new record of 57.4 gigatons of CO_2.[1] According to the United Nations, CO_2 emissions from fossil fuel combustion and industrial processes are the main contributors to the overall increase of 1.2% from 2021 to 2022, accounting for about two thirds of current greenhouse gas emissions. For this reason, it is of vital importance to work on the transition to alternative energy sources (solar, wind, biomass) that allow the reduction of GHG emissions and mitigate the environmental problems originating from the overexploitation of fossil resources.[2] Biomass-derived products have the necessary potential to be used in the current infrastructure to produce energy and chemicals.[3] In this context, lignocellulosic and non-lignocellulosic biomass can be transformed into hydrocarbons using different methods, *i.e.* carbonization, pyrolysis, gasification, and hydrothermal processing. Lignin can be converted into pyrolysis oil (bio-oil) through a rapid pyrolysis process. However, this bio-oil cannot be used directly as a fuel because of its high viscosity, low heating value and high oxygen content, resulting in a poor-quality oil.[4] The bio-oil derived from lignin is a complex mixture of hundreds of compounds with various functional groups, including hydroxyl (–OH), carbonyl (C=O), methoxy ($-OCH_3$) and carboxyl (–COOH) groups as well as unsaturated C=C bonds.[4] The removal of oxygen-containing groups from bio-oil by catalytic hydrodeoxygenation (HDO) is an important strategy for upgrading bio-oil to a high-quality hydrocarbon fuel.[5] Compounds such as anisole, phenol, guaiacol, catechol, syringol, and isoeugenol, among

[a]*Laboratorio de Nanocatálisis, Facultad de Química, Universidad Nacional Autónoma de México (UNAM), Cd. Universitaria, Coyoacán, C.P. 04510, Ciudad de México, Mexico. E-mail: klimova@unam.mx*
[b]*Instituto de Investigaciones en Materiales, Universidad Nacional Autónoma de México (UNAM), Cd. Universitaria, Coyoacán, C.P. 04510, Ciudad de México, Mexico*
† To the memory of Elena Klimova.

others, are representative model compounds of bio-oil and are frequently used in laboratory activity tests.[6]

The HDO catalytic process is used to reduce the oxygen content in bio-oil, where hydrogen is used to remove oxygen to form water or methanol and to hydrogenate aromatic rings and double bonds.[7] Various supported catalysts have been used in HDO, such as conventional hydrodesulfurization catalysts, *i.e.* alumina-supported sulfided CoMo and NiMo, which lead to fully deoxygenated products.[8] However, sulfur contamination and rapid deactivation due to coke formation occur with these catalysts. Supported noble metals, such as Pt, Pd, Rh and Ru, and reduced transition metals (Ni, Mo, Cu and W) have been widely used as active phases of monometallic HDO catalysts.[9,10] Jin *et al.*[11] evaluated nickel catalysts (10 wt%) supported on activated carbon, SBA-15, SiO_2, and γ-Al_2O_3 in the HDO of anisole at different temperatures (180–220 °C) and H_2 pressures (0.5–3.0 MPa). They concluded that Ni catalysts supported on silica materials showed better deoxygenation activity with high selectivity towards deoxygenated products (97% for Ni/SBA-15 and 95% for Ni/SiO_2). In the work of Wang *et al.*,[12] it was found that the HDO reaction of dibenzofuran over noble metal catalysts (Pt, Pd and Ru) supported on SBA-15 silica occurs first through the hydrogenation of aromatic rings followed by hydrogenolysis of the C–O bond to produce hydrocarbons. In that work, C–O bond cleavage took place at a higher temperature (280 °C). In addition, the increase in hydrogen pressure (0.5 to 5.0 MPa) promoted the saturation of the aromatic rings, influencing the conversion of DBF. A bimetallic PdRh/Al_2O_3 catalyst tested in the HDO of vanillin showed higher selectivity toward creosol (99%) than the monometallic Pd/C (the best of the monometallic catalysts, 71% selectivity) with a lower amount of consumed hydrogen.[13] Roldugina *et al.*[14] studied the HDO reaction of guaiacol in methanol with bimetallic PtPd and monometallic Ru catalysts supported on a mesoporous aluminosilicate of the Al-HMS(X) type with different Si/Al(x) ratios and on mesoporous zirconia modified with silica (m-ZrO_2–SiO_2). Guaiacol conversion on PdPt/m-ZrO_2–SiO_2 was higher (80%) than on PdPt/Al-HMS(10) (4%), which was attributed to a larger number of acid sites on the former catalyst's surface. Ru-containing catalysts exhibited higher activity in the HDO of guaiacol than PtPd-containing catalysts. The highest selectivity toward cyclohexanes was achieved on Ru/m-ZrO_2–SiO_2 and Ru/Al–HMS(10) catalysts (63 and 77%, respectively). Although supported noble metal catalysts were found to be the most suitable catalysts for HDO due to their double properties of metal and acidic sites,[15] the high cost of precious metals and the large amount of hydrogen required for complete removal of undesired compounds increase the total production and market costs of biofuels from pyrolysis bio-oils. On the other hand, conventional non-noble metal (Ni, Co, Fe)-supported catalysts are intensively used in the HDO of pyrolysis oil; however, they require higher operating temperatures and are more susceptible to rapid deactivation.[15] In recent years, research studies have been focused on the development of lower-cost catalysts to produce pyrolysis oil with similar properties to fossil fuels.[15] Along this line, studies of bimetallic catalysts containing noble and non-noble metals or a combination of two non-noble metals for the upgrading of biomass-derived pyrolysis bio-oil through HDO has intensified.[15] Thus, the non-noble bimetallic Co_8Ni_2/NC nanoalloy catalyst exhibited excellent catalytic activity, high selectivity and good stability towards vanillin HDO to obtain 2-methoxy-4-methylphenol, a promising method to upgrade biofuel.[16] The activation energy of vanillin alcohol over bimetallic catalysts was lower compared to that over monometallic Co or Ni catalysts, confirming that the synergetic effect between cobalt and nickel promotes high catalytic activity. Jin *et al.*[17] studied the promoting effect of Pt in Ni–Pt catalysts supported on activated carbon (AC) for the HDO of guaiacol. X-ray photoelectron spectroscopy characterization demonstrated strong Ni–Pt interactions in the bimetallic Ni–Pt/AC catalysts and their distinctive electronic features. These interactions create NiO_x vacancies that increase the Ni^0/Ni^{2+} ratio in the reduced Ni–Pt/AC catalysts by charge transfer from Pt to Ni, resulting in Pt^{2+} species coexisting with Pt^0 species. The combination of these effects facilitates the conversion of guaiacol, favoring the production of cyclohexanol and cyclohexanone particularly with the 14%Ni1%Pt/AC catalyst using methanol as a H_2 source. Faturachman *et al.*[18] studied bimetallic 10%Ni and 3%Pd supported on TiO_2 for the HDO of guaiacol with isopropyl alcohol as a H_2 source. They observed that the activity of the bimetallic Pd–Ni/TiO_2 catalyst was approximately two times higher in guaiacol conversion than Pd/TiO_2 and Ni/TiO_2 catalysts. Also, the bimetallic Pd–Ni/TiO_2 catalyst showed good selectivity to produce cyclohexanol, while Pd/TiO_2 was better for the production of phenolic compounds (2-methylphenol and phenol).[18] These differences were attributed to the adsorption capacity of the catalysts to dissociate hydrogen molecules, which is important for the HDO reaction.

The objective of this work was to contribute to a better understanding of the reaction mechanisms involved in HDO reactions in the presence of metallic catalysts of different nature (Ni, Pt, Pd and their bimetallic combinations) supported on an SBA-15-type material. In particular, we were interested in studying the effect of the combination of two metals (one noble with another non-noble) in forming bimetallic catalysts in order to inquire into a possible synergistic effect due to the interactions between these metals and their joint properties. To meet this objective, mono- and bimetallic catalysts were prepared, characterized and their activity and selectivity were evaluated in the HDO reaction of anisole as a representative model compound of quick pyrolysis bio-oil.

2. Experimental

2.1 Synthesis of the support

The mesoporous SBA-15 support was synthesized by the hydrothermal method described by Zhao *et al.*[19] Tetraethyl orthosilicate (TEOS, Aldrich) was used as the silica source, and triblock copolymer PEO_{20}-PPO_{70}-PEO_{20} (M_{av} = 5800 g mol^{-1}, Aldrich) as the templating agent. The typical procedure is as follows: 4 g

of the copolymer was dissolved in 30 mL of deionized water and stirred for 30 minutes, to which 120 mL of an aqueous solution of 2 M HCl was added and stirred moderately for 2 h, then the temperature of this solution was set to 35 °C and 8.5 g of TEOS was added dropwise, maintaining this temperature for 20 h. Finally, the temperature was increased to 100 °C and maintained for 24 h without stirring for the aging step. The white solid product was filtered, washed with deionized water and ethanol, dried at room temperature, and calcined at 550 °C for 6 h for the organic template removal.

2.2 Preparation of mono- and bimetallic catalysts

Bimetallic NiPd, NiPt and PdPt catalysts supported on SBA-15 were prepared by the conventional incipient wetness co-impregnation technique. Theoretical loadings of the metals in the catalysts were 5 wt% Ni, 1 wt% Pd, and 1 wt% Pt. The corresponding monometallic catalysts with the same metal loadings were also prepared for comparison purposes. Nickel nitrate ($Ni(NO_3)_2{\cdot}6H_2O$, Aldrich), palladium nitrate ($Pd(NO_3)_2{\cdot}2H_2O$, Aldrich) and hexachloroplatinic acid ($H_2PtCl_6{\cdot}6H_2O$, Aldrich) were used as precursors. After impregnation, the catalysts were first dried at room temperature for 24 h, then at 100 °C for 12 h (0.8 °C min^{-1} ramp) and calcined at 500 °C for 2 h (3 °C min^{-1}) under a static air atmosphere. The prepared catalysts were labeled as metal/S (Ni/S, Pt/S, Pd/S, NiPt/S, NiPd/S and PdPt/S).

2.3 Support and catalyst characterization

The SBA-15 support and the prepared catalysts were characterized by N_2 physisorption, low and wide-angle X-ray diffraction (XRD), UV-vis diffuse reflectance spectroscopy (DRS), temperature-programmed reduction (TPR), scanning electron microscopy-energy dispersive X-ray spectroscopy (SEM-EDS), high-resolution transmission electron microscopy (HRTEM) and scanning-transmission electron microscopy (HAADF-STEM).

2.3.1 Scanning electron microscopy. The chemical composition of the catalysts and elemental mappings were obtained by SEM-EDS analysis, using a JEOL 5900 LV microscope with OXFORD ISIS equipment. The samples were deposited on a carbon holder and evacuated at high vacuum.

2.3.2 Nitrogen physisorption. N_2 adsorption–desorption isotherms were obtained with a Micromeritics 3Flex automatic analyzer at liquid N_2 temperature (−197.5 °C). The samples were previously degassed at 270 °C for 10 h. Specific surface areas were calculated by the Brunauer–Emmett–Teller (BET) method (S_{BET}). The total pore volume (V_p) was determined by nitrogen adsorption at a relative pressure of 0.98 and pore size distributions were obtained from the adsorption and desorption isotherms by the Barrett–Joyner–Halenda (BJH) method. The reported mesopore diameters (D_{ads} and D_{des}) correspond to the maxima of the adsorption and desorption pore size distributions, whereas the micropore area (S_μ) was estimated using the correlation of t-Harkins & Jura (t-plot method).

2.3.3 X-ray diffraction. Powder XRD measurements were performed on a Siemens D5000 diffractometer, using CuKα radiation (λ = 1.5406 Å) and a goniometer speed of 1° (2θ) per minute. The XRD patterns of the samples were recorded from 3° to 80° (2θ). In addition, low-angle XRD patterns were obtained from 0.6° to 4° (2θ) on a Bruker D8 Advance diffractometer using small divergence and scattering slits of 0.05°.

2.3.4 UV-vis diffuse reflectance spectroscopy. UV-vis DR spectra of the samples were recorded using a Varian Cary 100 spectrophotometer equipped with a diffuse reflectance integrating sphere attachment for solid samples. Polytetrafluoroethylene was used as a reference material. The powder samples were loaded onto a Teflon cell with a quartz window and measured from 200 to 800 nm at room temperature. The Kubelka–Munk function was calculated from reflectance using $F(R) = (1 - R)^2/2R$.

2.3.5 Temperature-programmed reduction. TPR characterization experiments were implemented in a Micromeritics AutoChem II 2920 automatic analyzer equipped with a thermal conductivity detector. The catalysts were pre-treated thermally at 400 °C for 2 h in static air and then cooled down to room temperature. About 50 mg of catalysts were placed in the quartz reactor in a tubular furnace and the consumption of H_2 was recorded from 25 °C to 1000 °C (10 °C min^{-1}) under a stream of 10 : 90 molar ratio of H_2/Ar gas mixture (50 mL min^{-1} flow).

2.3.6 Transmission electron microscopy. Reduced catalysts were analyzed by transmission electron microscopy (TEM) using a JEOL 2010 microscope (resolving power 1.9 Å at 200 kV). The solids were ultrasonically dispersed in heptane and the suspension was collected on carbon-coated grids. TEM images were obtained from different parts of the samples. About 300 metal particles were measured in the images of each reduced catalyst to construct a frequency histogram of the particle diameter.

2.3.7 Scanning-transmission electron microscopy. The local structure of the reduced samples was determined by high-resolution scanning-transmission electron microscopy (STEM) in high-angle annular dark-field (HAADF) mode, using a Cs-corrected JEOL ARM-200F electron microscope, operated at 200 keV and located at Laboratorio Universitario de Microscopía Electrónica (LUME-UNAM, RRID:SCR_024400). The HAADF detector was set with convergence and collection semi-angles of ~24 mrad and 68–280 mrad, respectively. Energy-dispersive X-ray spectroscopy (EDS) was carried out with an Oxford AZtecTEM detector for acquiring area spectra and line scans of the different catalysts.

2.4 Catalytic tests

Prior to the catalytic activity tests, the catalysts were activated (reduced) *ex situ* in a U-shaped glass flow reactor at 400 °C for 4 h, under a stream of H_2/Ar (70 : 30 mol : mol) at atmospheric pressure. The hydrodeoxygenation of anisole was performed in a 300 mL stainless steel batch reactor (Parr), with a model solution of anisole (0.37 M, Aldrich, 99%) in hexadecane (Aldrich, 99%). In each activity test, 50 mL of anisole solution and 0.1 g of reduced catalyst were used. The hydrodeoxygenation of anisole was performed at 280 °C and 7.3 MPa total

pressure for 6 h while stirring at 500 rpm. Aliquots of the reaction mixture were taken every 15 minutes for the first hour, then every 30 minutes for the second hour and then every hour until the end of the reaction. The analysis of the aliquots was carried out in an Agilent 6890 gas chromatograph equipped with a flame ionization detector and a non-polar methyl siloxane capillary column HP-1 (50 m × 0.32 mm inner diameter and 0.52 μm film thickness). Product identification was performed on an Agilent 7890A GC system equipped with a 5975C MS detector. The catalytic activity was determined by measuring anisole concentrations at different times. The conversion of anisole (X_{AN}) was calculated as shown in eqn (1), where $C_{(AN)_0}$ is the initial anisole concentration (mol L^{-1}) in the reaction mixture and C_{AN} is the concentration of anisole (mol L^{-1}) at different reaction times t (h). Selectivity of products (S_i) was calculated as shown in eqn (2), where C_i is the concentration of the product i (mol L^{-1}) at time t:

$$X_{AN} = \frac{C_{(AN)_0} - C_{AN}}{C_{(AN)_0}} \times 100\% \quad (1)$$

$$S_i = \frac{C_i}{\sum_i C_i} \times 100\% \ . \quad (2)$$

3. Results and discussion

3.1 Characterization of calcined catalysts

3.1.1 Elemental analysis. The chemical compositions and elemental mappings of the prepared catalysts were obtained by the SEM-EDS method. The experimental compositions of the prepared catalysts are shown in Table 1. The catalysts have real metal loadings close to the theoretically expected ones. The elemental mapping results for mono- and bimetallic catalysts are shown in Fig. 1. It can be seen that, in each case, metals are uniformly distributed on the support's surface. With this, it was verified that the incipient wetness co-impregnation technique allows reaching a good distribution of each metal on the surface of the SBA-15 support.

3.1.2 Nitrogen physisorption. Fig. 2 shows the adsorption–desorption isotherms of the SBA-15 support and mono- and bimetallic catalysts. Textural characteristics are shown in Table 1. The SBA-15 support exhibited a type IV nitrogen adsorption–desorption isotherm corresponding to mesoporous solid materials, according to the IUPAC classification.[20] The H1 hysteresis loop of the SBA-15 support is associated with the presence of uniform cylindrical pore channels. All the prepared mono- and bimetallic catalysts preserved the characteristic shape of the isotherm of the SBA-15 support (see Fig. 2).

Specific textural characteristics (S_{BET}, S_μ, V_P, D_{ads} and D_{des}) of the SBA-15 support and catalysts are shown in Table 1. The BET surface area and total pore volume of the catalysts were smaller than those of the starting SBA-15 support, which could be partially attributed to the incorporation of each metal on the surface of the support and the increase in the density of the catalysts compared to the support. However, a decrease in the BET surface area was between 8 and 17% for monometallic catalysts and between 10 and 18% for the bimetallic ones. This decrease in the surface area is larger than the increase in the samples' density due to metal deposition. Therefore, some pore blocking could be expected in the calcined catalysts by the agglomerated metal particles.

Fig. 3 shows the pore diameter distributions obtained from the adsorption and desorption branches of the isotherms of the SBA-15 support and mono- and bimetallic catalysts. All the pore distributions were monomodal and uniform with the pore size maxima located at about 8.7–8.8 nm for the adsorption distributions and about 6.6–6.7 nm for the desorption ones. A slight decrease in the pore diameter was observed only for the Ni/S catalyst, pointing to the deposition of nickel oxide species inside the SBA-15 mesopore channels.

3.1.3 X-ray diffraction. Fig. 4(A) shows the low-angle diffractograms (0.6–4.0° 2θ) of the SBA-15 support and calcined catalysts. The SBA-15 support exhibits well-defined diffraction

Table 1 Elemental composition, and textural and structural characteristics of the support and catalysts

	Elemental composition[a]			Textural and structural characteristics[b]						
	Experimental (wt%)									
Material	Ni	Pd	Pt	S_{BET} ($m^2\ g^{-1}$)	S_μ ($m^2\ g^{-1}$)	V_P ($cm^3\ g^{-1}$)	D_{ads} (nm)	D_{des} (nm)	a_0 (nm)	δ (nm)
SBA-15	—	—	—	722	51	1.23	8.8	6.7	11.7	2.9
Ni/S		5.04	—	599	53	1.04	8.5	6.6	11.3	2.8
Pd/S	—	1.05	—	661	51	1.12	8.7	6.6	11.5	2.8
Pt/S	—	0.83	—	668	55	1.13	8.8	6.7	11.3	2.6
NiPd/S	4.46	0.81		604	42	1.03	8.6	6.6	11.2	2.7
NiPt/S	5.05		1.01	595	51	0.99	8.6	6.6	11.3	2.8
PdPt/S		0.81	0.66	653	53	1.10	8.7	6.7	11.3	2.6

[a] Determined by SEM-EDS. Nominal compositions of the catalysts were 5 wt% Ni and 1 wt% Pd or Pt. [b] S_{BET}, specific surface area; S_μ, micropore area; V_P, total pore volume; D_{ads} and D_{des} mesopore diameters corresponding to the maxima of the pore size distributions calculated from adsorption and desorption isotherms, respectively; a_0, unit-cell parameter calculated from the position of the (100) diffraction peak ($a_0 = 2 \cdot d_{100}/\sqrt{3}$); δ, pore wall thickness of SBA-15 materials calculated by subtraction of adsorption pore diameter D_{ads} from the unit cell parameter (a_0).

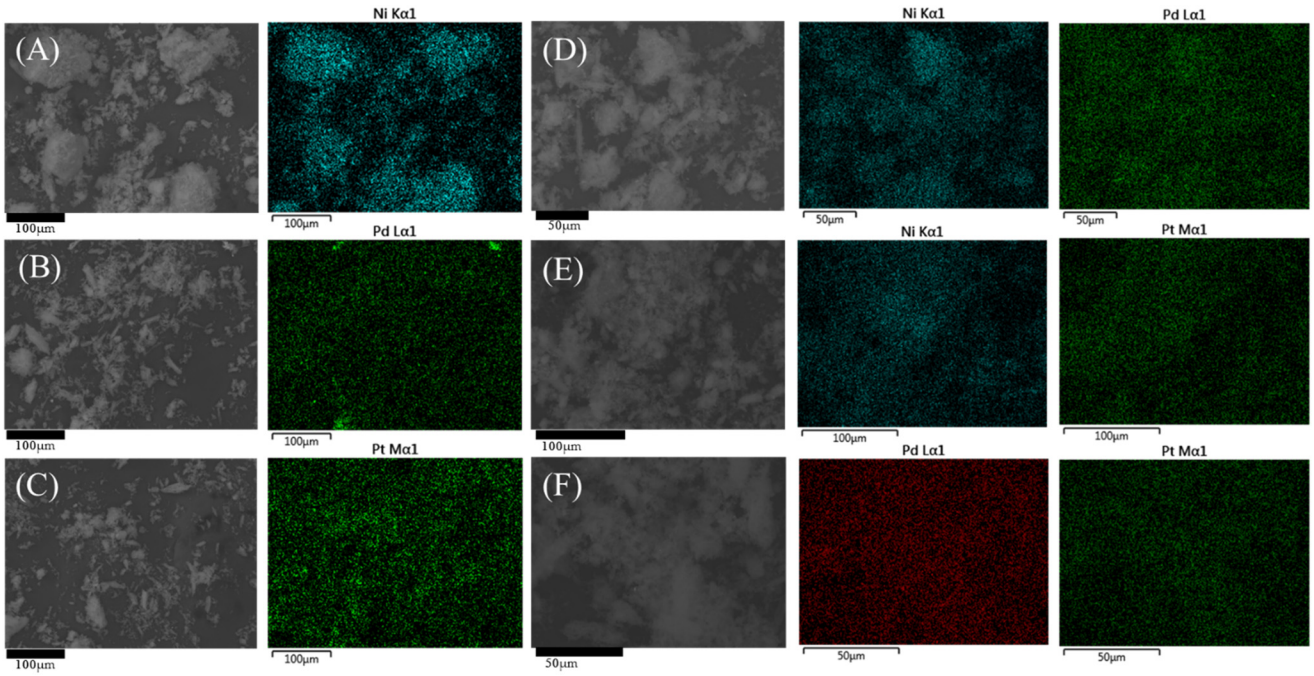

Fig. 1 Elemental mappings of the catalysts: (A) Ni/S; (B) Pd/S; (C) Pt/S; (D) NiPd/S; (E) NiPt/S; and (F) PdPt/S.

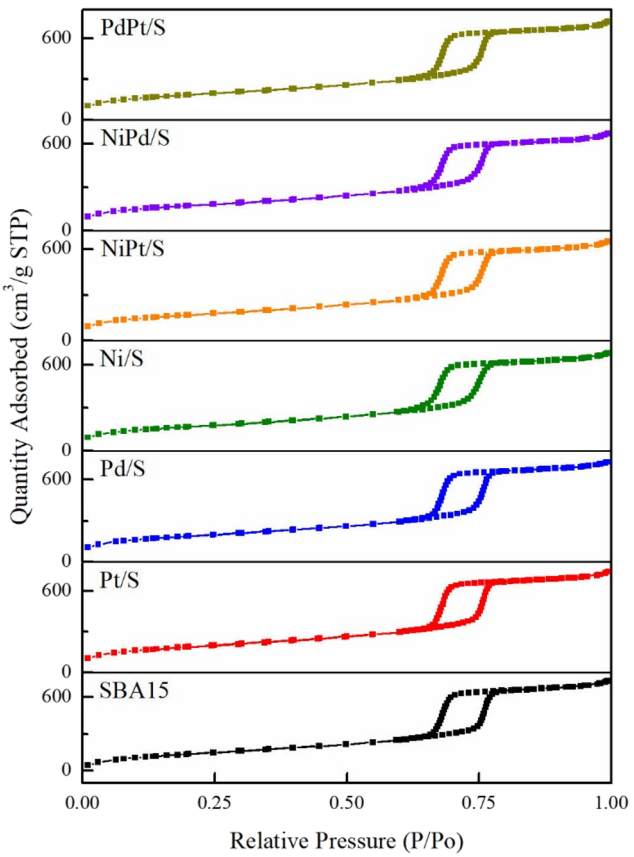

Fig. 2 N_2 adsorption–desorption isotherms of the SBA-15 support and calcined catalysts.

angles at 0.9, 1.5 and 1.7° (2θ) typical of the hexagonal pore structure ($p6mm$), which are associated with the (100), (110) and (200) planes, respectively. In this two-dimensional hexagonal pore arrangement, one central pore is surrounded by six other pores of the same size. These diffraction angles can also be observed in the diffraction patterns of all mono- and bimetallic catalysts. Therefore, the hexagonal pore structure of the SBA-15 support is maintained even after the synthesis of the catalysts. The pore wall thickness (δ) was determined using the unit-cell parameter (a_0) determined from the position of the (100) reflection and the adsorption pore size (D_{ads}) obtained by nitrogen physisorption (Table 1). According to the results, the unit-cell parameter of mono- and bimetallic catalysts was just slightly smaller (0.2–0.5 nm) than that of the starting SBA-15 support, while the pore wall thickness of the catalysts changed between 2.6 and 2.8 nm, close to the 2.9 nm value of the SBA-15 support. These results mean that the mechanical and thermal resistance of the support was maintained in the prepared catalysts, as well as the shape, structure, and size of the mesoporous structure of the support.

Fig. 4(B) shows the results of wide-angle powder X-ray diffraction analysis (10–80° 2θ) of the SBA-15 support and calcined catalysts. The SBA-15 support shows a broad signal between 15 and 36° (2θ) that corresponds to amorphous silica. This signal is also present in the diffraction patterns of all prepared catalysts. In addition, for Ni-containing catalysts (Ni/SBA-15, NiPd/SBA-15 and NiPt/SBA-15) four signals were observed at 37.25, 43.28, 62.98 and 75.63° (2θ) corresponding to the (111), (200), (220) and (311) planes of the crystalline cubic ($Fm\bar{3}m$) phase of nickel oxide (NiO, JCPDS-ICDD card 01-071-1179). For Pd-containing catalysts (Pd/SBA-15, NiPd/SBA-15 and PdPt/SBA-15),

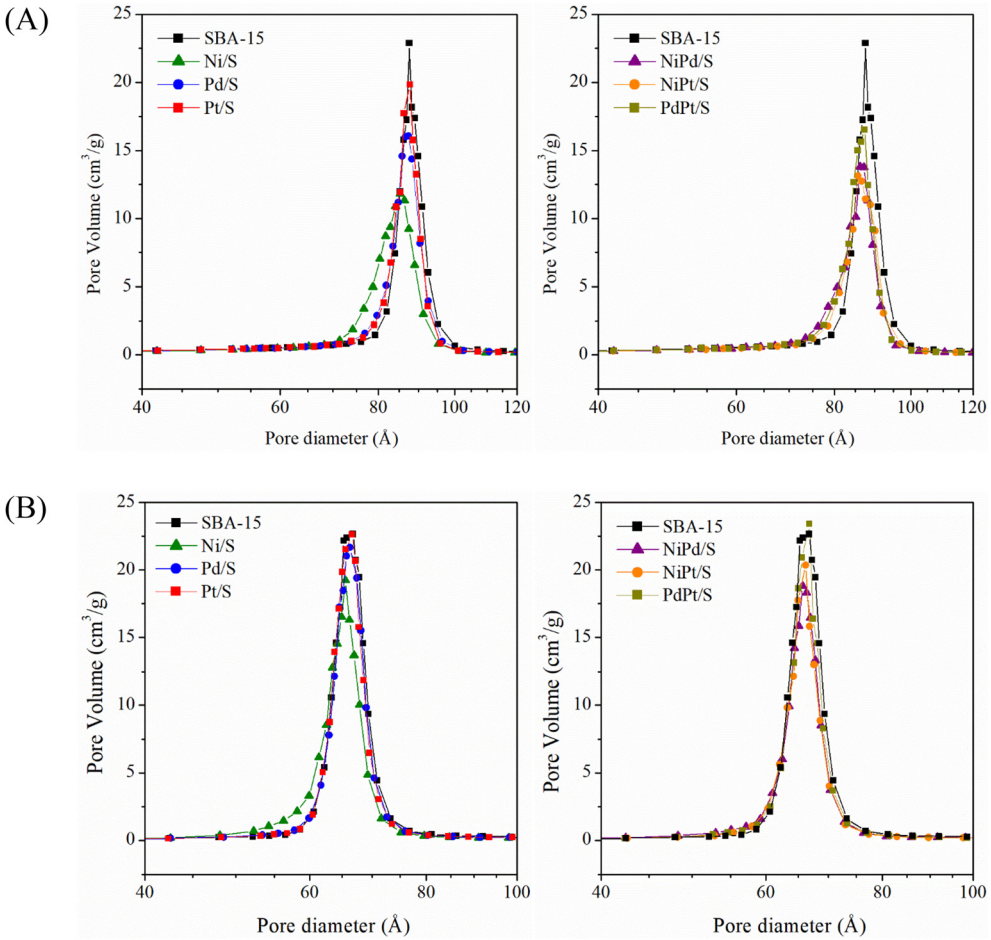

Fig. 3 Pore size distributions of the support and catalysts obtained from (A) adsorption isotherms and (B) desorption isotherms.

signals were observed at 33.90, 41.80, 54.82, 60.39 and 71.57° (2θ) corresponding to the (101), (110), (112), (103) and (211) planes of the crystalline tetragonal (*P*42/*mmc*) phase of palladium oxide (PdO, JCPDS-ICDD card 00-043-1024). For Pt-containing catalysts, some differences were detected in the diffraction patterns. Thus, for the Pt/SBA-15 and bimetallic PdPt/SBA-15 catalysts, the signals of the crystalline cubic ($Fm\bar{3}m$) platinum phase (Pt, JCPDS-ICDD card 00-004-0802) were observed at 39.77, 46.31 and 67.52° (2θ) assigned to the (111), (200) and (220) planes, respectively. No signals indicating the presence of any crystalline phase of platinum oxide were observed. This coincides with observations by other authors[21–23] indicating that the Pt^{4+} species of the hexachloroplatinic acid ($H_2PtCl_6{\cdot}6H_2O$) used as a precursor were reduced during catalyst preparation. On the other hand, in the diffraction pattern of the bimetallic NiPt/SBA-15 catalyst, no Pt signals were observed, as has been reported previously in work by other authors.[24] This could be attributed to wide dispersion of Pt species in this catalyst due to the interaction with the NiO, making these Pt species undetectable by XRD analysis.

Fig. 4 also shows the crystallite sizes of different crystalline phases found in calcined catalysts estimated using the Scherrer equation. It can be noted that, in general, the crystallite size of NiO, PdO and Pt phases is smaller in the bimetallic catalysts compared to the monometallic ones (Ni/S, Pd/S and Pt/S). An exception to this rule is found with the NiPt/S catalyst, in which the crystallite size of the NiO phase increased in the presence of Pt and, meanwhile, the separate Pt crystalline phase was not detected. The above suggests that there is a possibility of the formation of a mixed NiO–Pt phase, where Pt atoms are included inside the NiO particles, increasing their size.

3.1.4 UV-vis diffuse reflectance spectroscopy (UV-vis DRS). UV-vis DRS spectra of the catalyst are shown in Fig. 5. The Ni/S catalyst exhibits three characteristic bands of Ni^{2+} in octahedral coordination. The band observed in the ~200 to 350 nm range is associated with the ligand to metal charge transfer (LMCT), which occurs from the 2p orbitals of the oxygen to the Eg orbitals of NiO (Ni^{2+}) in octahedral coordination. The lower intensity bands at 420 nm and 725 nm correspond to d–d electronic transitions of nickel (Ni^{2+}).[25] These bands of octahedral nickel oxide species are also visible for the bimetallic NiPt/S and NiPd/S catalysts. Regarding the Pt/S catalyst, a low-intensity signal at the visible light region

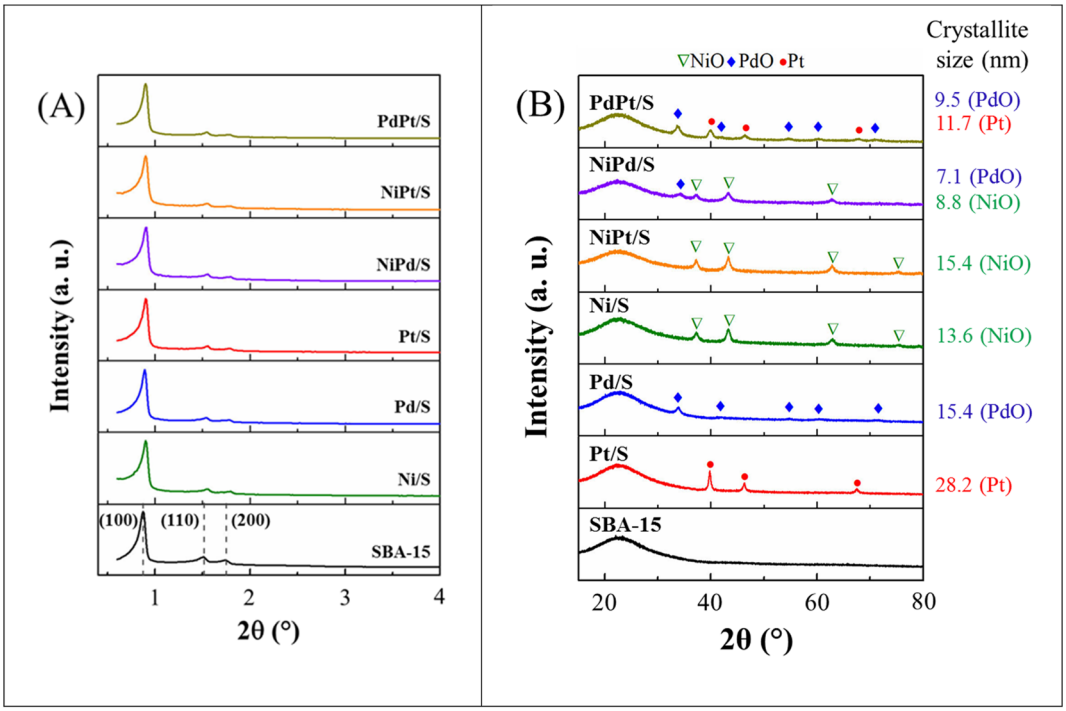

Fig. 4 (A) Low-angle and (B) wide-angle powder X-ray diffraction patterns of the SBA-15 support and prepared catalysts.

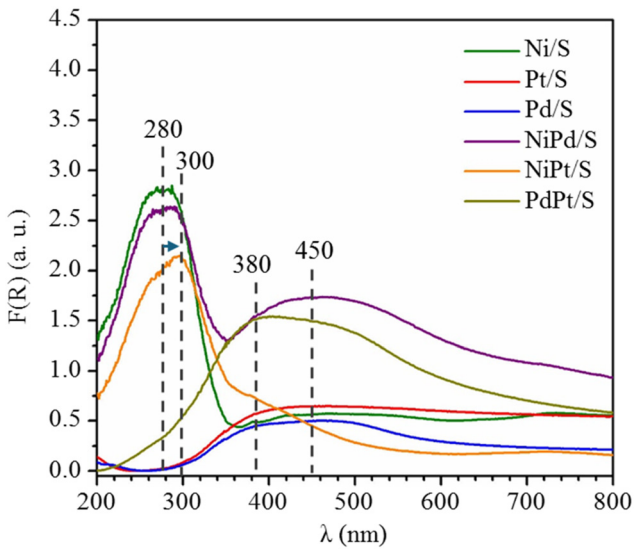

Fig. 5 UV-vis diffuse reflectance spectra of calcined catalysts.

(400–700 nm) points out the presence of metallic Pt nanoparticles in the Pt/S catalyst.[26] This is in line with the XRD results of this catalyst where the metallic Pt crystalline phase was detected, as shown in Fig. 4(B). On the other hand, a characteristic signal at 263 nm corresponding to the $[PtCl_6]^{2-}$ species of the platinum precursor used[27] was not observed in the spectrum of our Pt/S catalyst. Also, the results obtained from SEM do not indicate the presence of Cl in the Pt/S catalyst (Table 1). For the Pd/S and NiPd/S catalysts, a very low intensity absorption band at ~210 nm was observed. This band could be attributed to the dπ–pπ charge transfer transition between Pd and oxygen of the small PdO particles.[28] For Pd/S and NiPd/S catalysts, a broad band at wavelengths from 350 to 550 nm, centered at ~450 nm, was observed. This broad band is attributed to relatively large PdO particles or their agglomerates,[29,30] in agreement with XRD observations. In the spectrum of the NiPd/S catalyst, signals observed in the spectra of monometallic Ni/S and Pd/S catalysts overlap. No clear differences in the bands corresponding to NiO and PdO species were detected in the spectra of the bimetallic NiPd/S catalyst and its monometallic Ni/S and Pd/S analogs. On the other hand, some changes can be detected in the spectrum of the NiPt/S catalyst, when compared to those of their monometallic Ni/S and Pt/S counterparts. Thus, the most intense band between 200 and 350 nm associated with the LMCT of NiO and the corresponding absorption edge were slightly red shifted probably due to a slight increase in the NiO particle size. At the same time, a shoulder observed at 380 nm in the spectrum of the NiPt/S catalyst should correspond to metallic Pt species with a size significantly smaller than that in the monometallic Pt/S catalyst.

3.1.5 Temperature-programmed reduction. TPR profiles of the calcined catalysts are shown in Fig. 6. Reduction of NiO takes place in one step ($NiO + H_2 \rightarrow Ni + H_2O$). Based on this, two principal reduction peaks are observed in the reduction profile of the Ni/S catalyst at 294 and 420 °C that could be associated with the presence of two different nickel oxide species. The first reduction peak (at 294 °C) could be ascribed to the reduction of free NiO species in weak interaction with

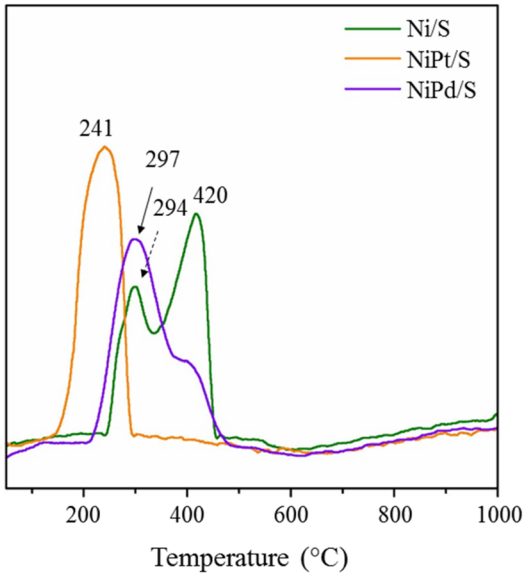

Fig. 6 TPR profiles of selected calcined catalysts supported on SBA-15.

the silica support. Such NiO crystallites were detected by powder XRD and, according to their size (13.6 nm, Fig. 4(B)), are located on the external surface of the SBA-15 support. The second higher intensity signal of hydrogen consumption between 350 and 450 °C (maximum at 420 °C) is ascribed to the reduction of NiO species in stronger interaction with the silica support. Probably these species are located inside the mesoporous channels of the SBA-15.[31,32] Reduction of PdO species in the Pd/S catalyst should also occur in a single step ($PdO + H_2 \rightarrow Pd + H_2O$). However, in the TPR profiles (not shown) of the Pd/S and Pt/S catalysts, a well-defined reduction peak was not detected. Previously it was observed that palladium oxide, which is in very weak interaction with the inert SBA-15 silica material, such as in the Pd/S catalyst, is easily reduced at low temperatures (at around 0 °C).[30,33] On the other hand, a low-intensity negative signal of H_2 evolution at about 60 °C observed in the TPR profile of the Pd/S catalyst can be attributed to the decomposition of previously formed palladium hydrides.[30,33] For the Pt/S catalyst, the absence of reduction signals in the corresponding TPR profile is in line with the presence of metallic platinum after calcination of this catalyst at 500 °C as shown by XRD. The addition of Pd to the Ni/S catalyst resulted in a noticeable increase in the proportion of NiO species reducible at low temperatures (~297 °C) and a decrease in NiO species that reduce at about 410 °C (Fig. 6). These changes in the TPR profile of the bimetallic NiPd/S catalyst compared to its monometallic Ni/S counterpart could be attributed to the fact that PdO species reduced at low temperatures (50–100 °C) can promote the reduction of NiO species by dissociative chemisorption of hydrogen on reduced Pd species.[32] In contrast to the TPR profile of the bimetallic NiPd/S catalyst, for the bimetallic NiPt/S analog, only one reduction peak was detected at 241 °C (Fig. 6). This peak suggests that the presence of metallic platinum in the NiPt/S catalyst and a possible interaction between Ni and Pt species can significantly facilitate the reduction of NiO by hydrogen activation on Pt species and their further spillover to NiO moieties.[24,34] For the bimetallic PdPt/S catalyst, no reduction signals were observed, and it is assumed that PdO species were reduced at low temperatures (around 0 °C or below). A low-intensity negative signal observed around 600 °C was attributed to the desorption of hydrogen strongly chemisorbed on metallic Pd and Pt species.

3.2 Characterization of reduced catalysts

3.2.1 X-ray diffraction. Fig. 7(A) shows the XRD patterns of catalysts reduced at 400 °C for 4 h and the crystallite sizes of metal nanoparticles estimated using the Scherrer equation. For Ni/S, NiPt/S and NiPd/S catalysts, no signals corresponding to the NiO crystalline phase were observed. Instead, three reflections appeared at 44.25, 51.79 and 76.81° (2θ) corresponding to the (111), (200) and (220) planes of the crystalline cubic phase of metallic nickel (Ni^0) (JCPDS-ICDD card 01-071-4655). In the NiPd/S catalyst, the signals of metallic Ni were less defined and of lower intensity than those in the patterns of other Ni-containing reduced catalysts. This can be due to a better dispersion of Ni crystals (5 nm crystallite size) in this catalyst, induced by the presence of Pd compared to the Ni/S sample (8.7 nm) and the NiPt/S one (10.4 nm).

For the monometallic Pd/S catalyst, three signals were detected at 40.11, 46.62 and 68.15° (2θ) assigned to the (111), (200) and (220) planes of the crystalline cubic phase of metallic Pd (JCPDS-ICDD card 00-005-0681). For the NiPd/S catalyst, the signals of the metallic palladium phase slightly moved to higher 2θ values of 40.99, 47.6 and 69.88° (2θ), reflecting a decrease in the unit cell parameter value (interplanar distances of the Pd phase, Fig. 7(B)). This shift can be attributed to the incorporation of some smaller Ni atoms into the metallic Pd phase and/or to the formation of bimetallic Ni–Pd particles. Additionally, as mentioned above, the dispersion of Ni species in this bimetallic catalyst was better than that in its monometallic Ni/S analog (see Fig. 7(B)). According to Hume-Rothery rules,[35] Pd has a lower surface tension and a larger atomic radius than Ni, which would make the formation of a Pd–Ni alloy difficult. However, according to the effective-medium theory (EMT)[36] and thermodynamics for small systems,[37] the energies of segregation and surface mixing for transition metals suggest that a combination of Pd and Ni atoms can exist in the form of a mixture where Pd tends to be released from the matrix of Ni leading to a strong segregation of Pd towards the metal surface.

The monometallic Pt/S catalyst, after reduction, shows the same diffraction peaks (39.77, 46.31 and 67.52° 2θ) as the calcined catalyst (Fig. 4(B)) since Pt had already been reduced during catalyst preparation. For the reduced bimetallic NiPt/S catalyst, the presence of only the metallic Ni phase was observed, while the signals of the metallic Pt crystalline phase were absent. In addition, diffraction peaks of Ni^0 were slightly shifted to the smaller 2θ values compared to those of the monometallic Ni/S catalyst, as shown in Fig. 7(C). This

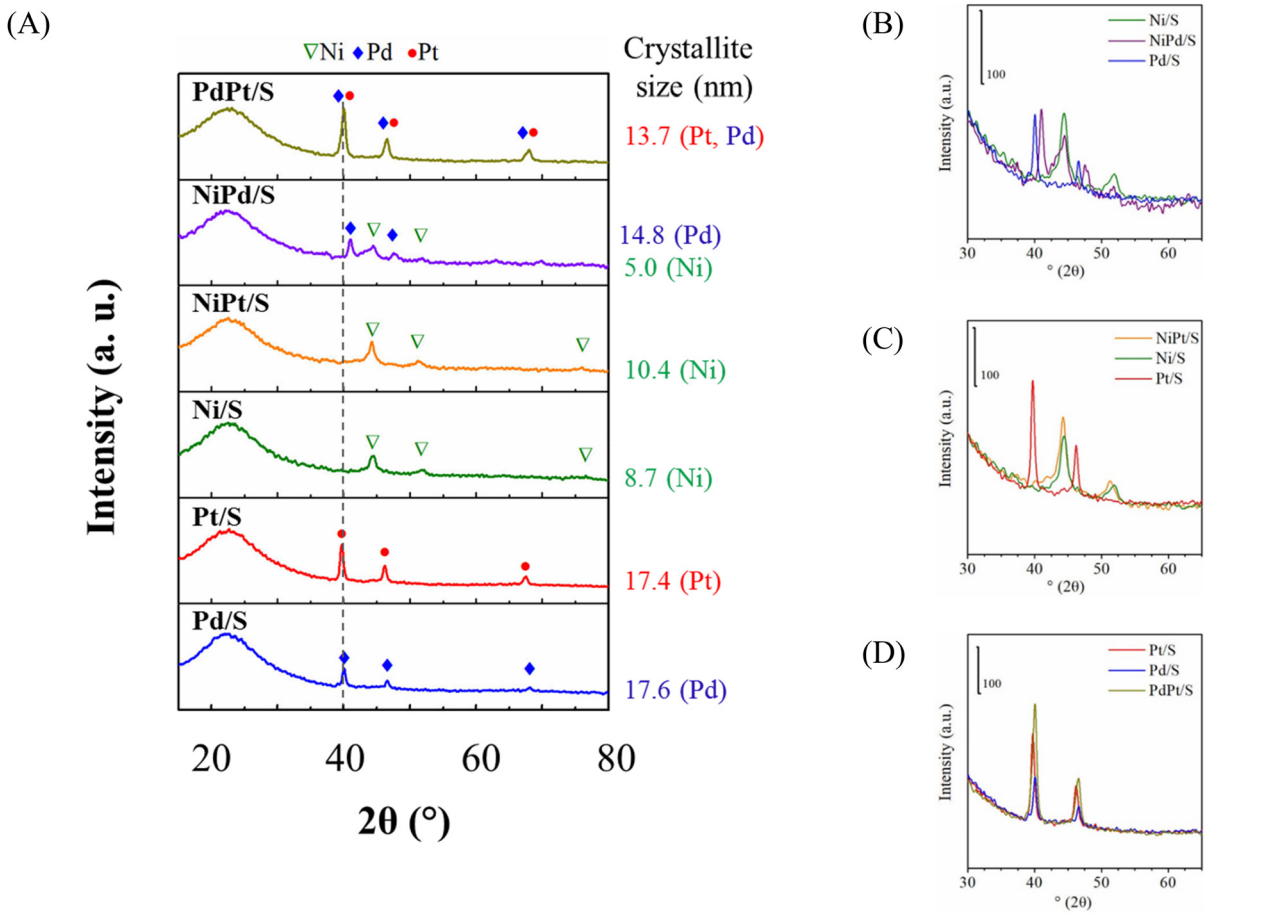

Fig. 7 (A) Powder XRD patterns of reduced catalysts. Comparison of XRD patterns of (B) Ni/S, NiPd/S and Pd/S catalysts; (C) Ni/S, NiPt/S and Pt/S catalysts; (D) Pt/S, PdPt/S and Pd/S catalysts.

suggests the formation of Ni–Pt bimetallic particles.[34] According to the EMT theory, in this case the energies of segregation and surface mixing between Pt and Ni allow non-segregated mixing of Pt and Ni with the incorporation of larger Pt atoms into the Ni matrix. On the other hand, the existence of some small metallic Pt particles (<5 nm size) not detectable by the XRD technique in the reduced NiPt/S catalysts cannot be ruled out.

For the reduced bimetallic PdPt/S catalyst, three well-defined signals were observed at 40.03, 46.52 and 68.01° (2θ). These reflections are located between the 2θ values of pure Pd^0 and Pt^0 crystalline phases. For example, the most intense (111) signal of the PdPt/S catalyst is observed at 40.03° (2θ), where this signal is located in an intermediate position between 40.11° and 39.77° (2θ) for metallic Pd and Pt, respectively (Fig. 7(D)). This could indicate a close interaction between the two metals.[38] Considering the similar characteristics of Pd^0 and Pt^0 fcc crystal structures and similar lattice constants, the formation of an alloy between these metals is possible.[39,40] Three reflections observed by us for the PdPt/S catalyst are similar to those reported previously for the $Pd_{0.25}Pt_{0.75}$ alloy (JCPDS 04-017-6714) and correspond to the (111), (200), and (220) crystal planes, respectively. These results are in line with a recent report[41] where Pd–Pt alloying was detected for PdPt/Al/SBA-15 catalysts.

3.2.2 TEM characterization. The reduced mono- and bimetallic Ni, Pd and Pt catalysts were examined by TEM. Fig. 8 shows the obtained micrographs. In general, the pore structure of the SBA-15 support and the deposited metallic nanoparticles can be observed in the images. Metal nanoparticles have different sizes and are mainly round or oval shaped (Fig. 8). The majority of the observed nanoparticles are larger than the SBA-15 mesopores and are located on the external surface of the SBA-15 porous structure. However, some smaller nanoparticles could also be found and it seems that they are deposited inside the cylindrical pores of the SBA-15 material, as shown in Fig. 8(D and E). These nanoparticles have a size slightly smaller than the SBA-15 mesopores and they are aligned in the ordered cylindrical mesopores of the SBA-15 material. The presence of two types of such metal nanoparticles has been reported recently for the Pd/Al-SBA-15 catalysts[42] and bimetallic PdPt/Al/SBA-15 catalysts.[41]

Several images of each reduced catalyst were used to measure the metal particle size in the reduced mono- and bimetallic Ni/S, Pd/S, Pt/S, NiPd/S, NiPt/S and PdPt/S catalysts to construct the corresponding particle size distributions. Fig. 9

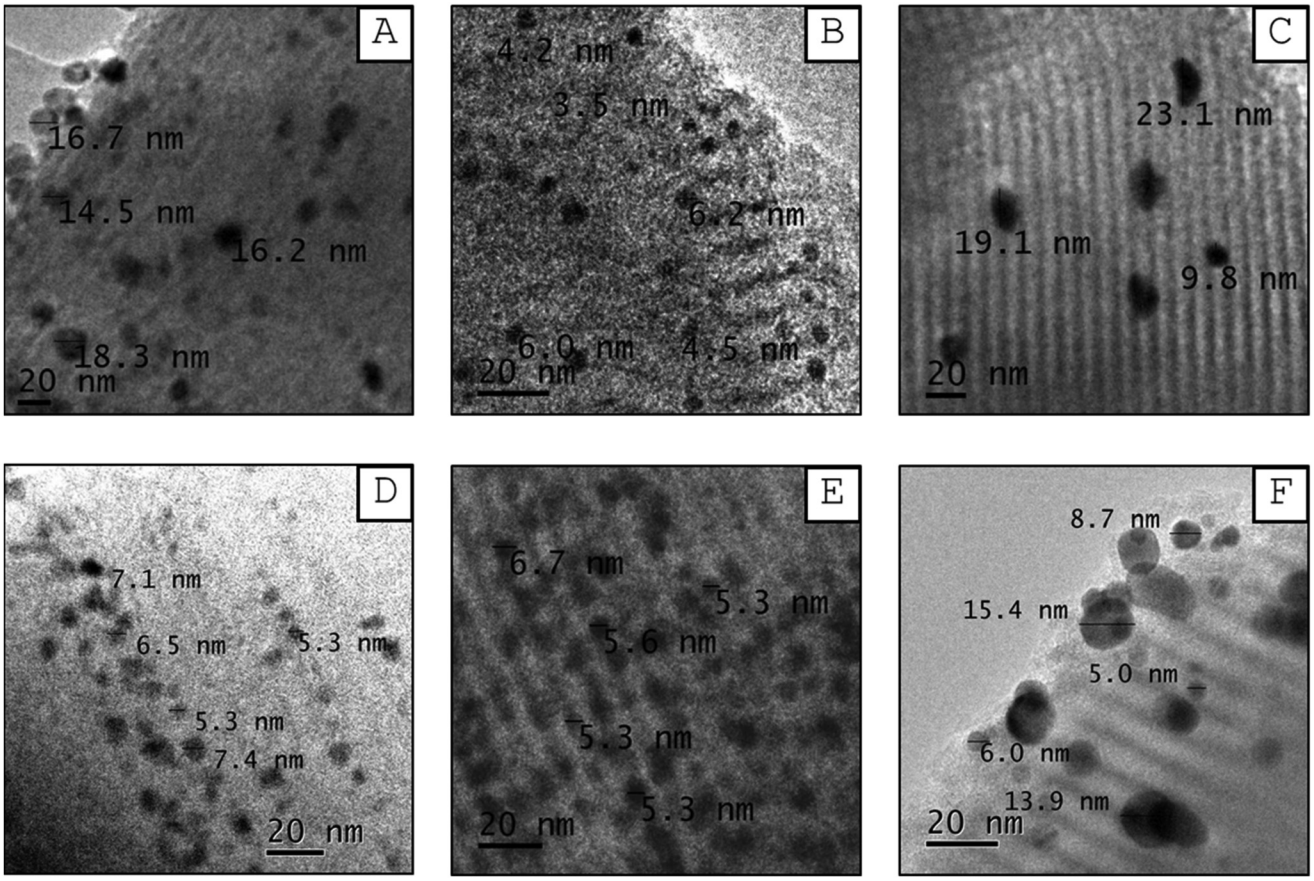

Fig. 8 TEM micrographs of reduced catalysts: (A) Ni/S, (B) Pd/S, (C) Pt/S, (D) NiPd/S, (E) NiPt/S, and (F) PdPt/S.

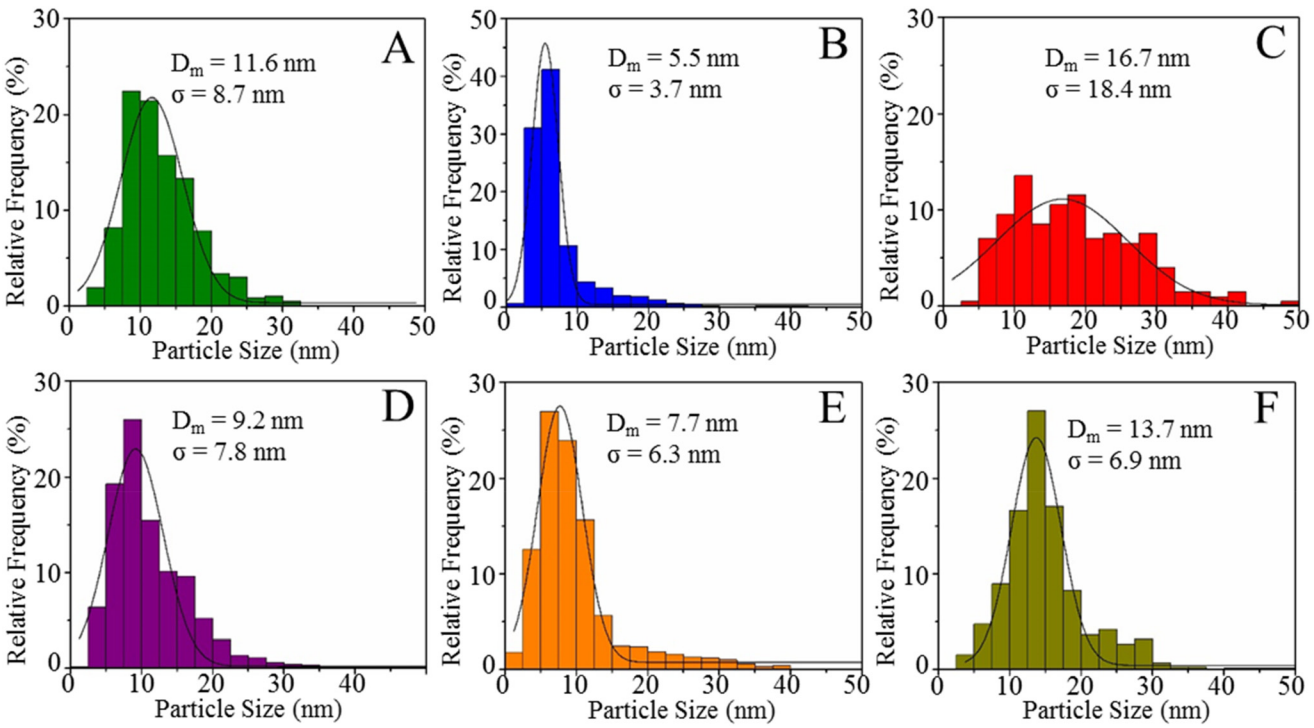

Fig. 9 Particle-size distribution histograms of reduced mono- and bimetallic catalysts: (A) Ni/S, (B) Pd/S, (C) Pt/S, (D) NiPd/S, (E) NiPt/S, and (F) PdPt/S.

shows the obtained particle size distributions, the mean particle sizes (D_m) and standard deviations (σ). The mean metal particle size increases in the following order: Pd/S (5.5 nm) < NiPt/S (7.7 nm) < NiPd/S (9.2 nm) < Ni/S (11.6 nm) < PdPt/S (13.7 nm) < Pt/S (16.7 nm). Among monometallic catalysts, the Pd/S showed the smallest mean particle size, while for the bimetallic ones, it was NiPt/S. On the other hand, the standard deviation values increase as follows: Pd/S (3.7 nm) < NiPt/S (6.3 nm) < PdPt/S (6.9 nm) < NiPd/S (7.8 nm) < Ni/S (8.7 nm) < Pt/S (18.4 nm). According to the particle size distributions shown in Fig. 9, the Pd/S catalyst had the narrowest distribution, with particles mainly ranging from 2.5 to 10 nm, while the Pt/S had the widest distribution of particles of heterogeneous sizes between 5 and 32.5 nm.

The metal dispersion in the reduced catalysts was estimated based on the mean particle size determined from the particle size distributions obtained with the TEM micrographs using the Borodziński and Bonarowska method.[43] The dispersion values increase as follows: Pt/S (8.3%) < PdPt/S (10.1%) < Ni/S (10.8%) < NiPd/S (13.7%) < NiPt/S (16.4%) < Pd/S (25.0%).

3.2.3 HAADF-STEM characterization. The reduced bimetallic catalysts were analyzed by HAADF-STEM to corroborate their local structure, and determine the interaction between their constituent metals. The low-magnification images of the NiPd/S catalyst in Fig. 10(A and B) show that small nanoparticles were dispersed along the entire SBA-15 material, and they were located mainly in the pore structure. The presence of some larger particles was evident.

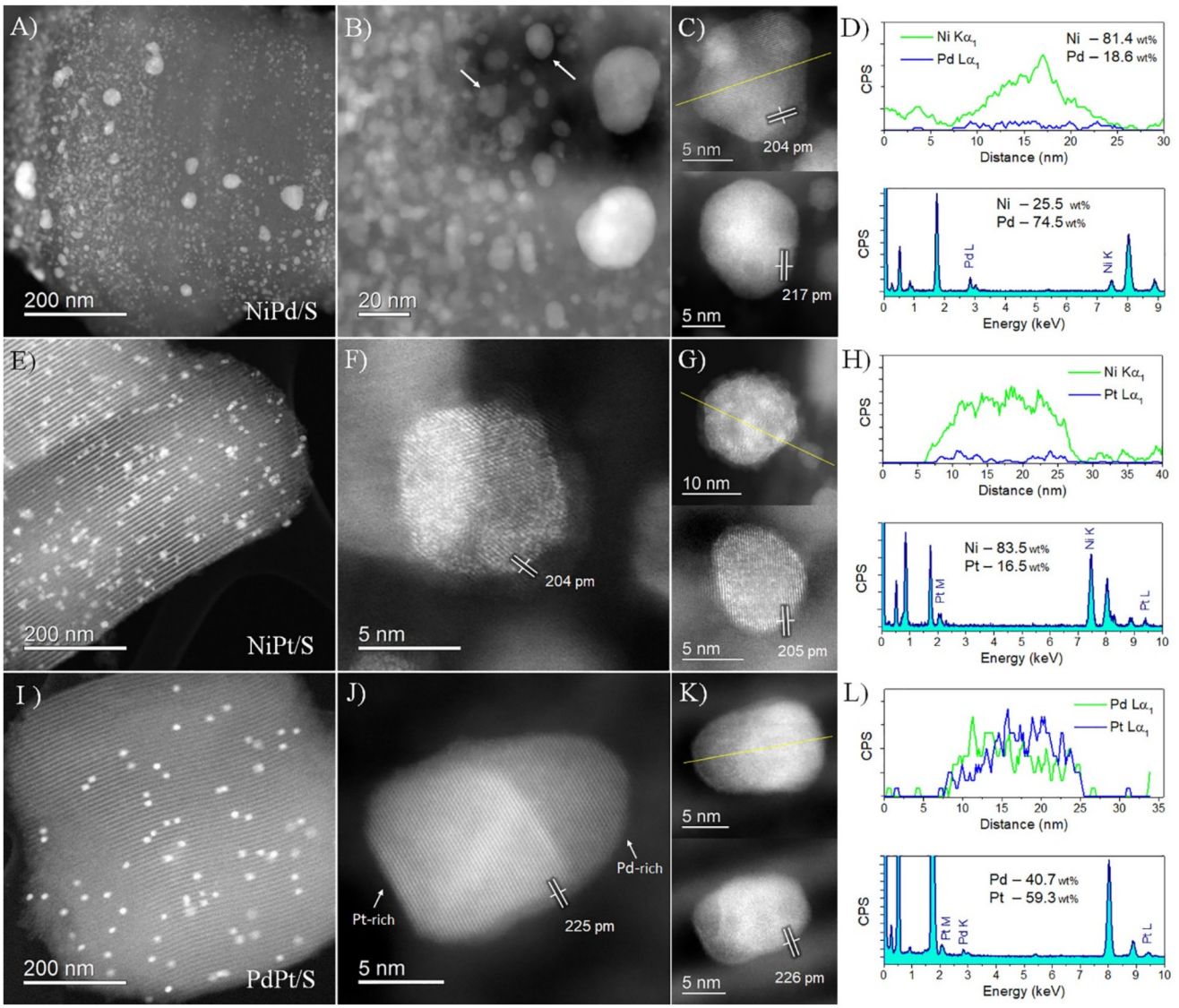

Fig. 10 HAADF-STEM images and EDS analyses of the bimetallic catalysts. (A–D) NiPd/S, (E–H) NiPt/S, and (I–L) PdPt/S. Upper graphs in panels D, H, and L correspond to EDS line-scans acquired along the yellow lines in panels C, G and K, respectively, while the graphs in the lower part of panels D, H, and L correspond to average EDS spectra.

The nature of the particles was determined from the lattice-resolution images and EDS analyses. Fig. 10(B and C) shows representative images of the particles. One particle exhibited lattice fringes of 204 pm, corresponding to the {111} planes of the Ni structure, while a larger particle showed a larger lattice spacing of 217 pm, corresponding to the {111} planes of a Pd-rich particle. This representative result indicates a non-homogeneous chemical composition of the particles. EDS confirmed this idea. The EDS line scan (Fig. 10(D), upper graph) across the upper particle shown in Fig. 10(C) revealed that the particle was composed mainly of Ni, with a small proportion of Pd. In contrast, the EDS spectrum of the lower particle shown in Fig. 10(C) confirmed its Ni–Pd_{rich} composition. In fact, based on EDS analyses performed on different areas, it was found that small particles were composed mainly of Ni, while larger particles presented a Pd-rich composition. These results are in agreement with XRD analysis in which phase segregation was detected where separated peaks corresponding to Ni and Pd phases were observed that have different particle sizes (Fig. 7).

NiPt/S catalysts, in turn, showed better distribution of particles on the support, as revealed in Fig. 10(E). The atomic-resolution HAADF images revealed the location of Pt on the particles (Fig. 10(F and G)), clearly indicated by the higher contrast produced by its higher atomic number (Z = 78) compared to Ni (Z = 28). Lattice fringes of 204–205 pm matched the {111} planes of Ni, indicating low Pt incorporation into the crystal structure. No small Pt particles were detected; instead, the sample consisted of Pt-decorated nanoparticles, with Pt atoms well dispersed and segregated on the surface, in agreement with the previously described XRD analysis. The EDS analysis confirmed the presence of Pt at a low concentration compared to Ni (Fig. 10(H)), with the highest Pt concentration of up to 16.5 wt%.

Finally, the PdPt/S sample presented the largest particle size of the bimetallic catalysts. This led to less dispersed particles on the SBA support, as noticed in Fig. 10(I). The atomic-resolution HAADF images confirmed the local structure of these PdPt nanoparticles (Fig. 10(J and K)). It is noticed that the particles are different compared to the other catalysts, with elongated shapes apparently following the channel structure of the support. The measured lattice fringes of 225–226 pm matched the {111} planes of Pd and Pt; however, the distinction between both structures from their lattice spacings is unfeasible because of the highly similar cell parameters. This complication was surpassed by HAADF imaging due to the considerable difference in atomic number between Pt (Z = 78) and Pd (Z = 46). It is observed that the nanoparticles consisted of a PdPt alloy but with considerable elemental segregation. This segregation pattern formed a kind of Janus-type configuration in which high- and low-contrast areas correspond to Pt-rich and Pd-rich interacting areas in the particle structure, respectively. In this nanosystem, as the melting temperature of both elements is very similar, the second segregation rule applies, and the lower surface energy of Pd compared to Pt induces Pd segregation to the surface.[44] The EDS line scan shown in Fig. 10(L) confirmed this elemental segregation. The average chemical composition of the local area corresponded to Pd at 40.7 wt% and Pt at 59.3 wt%.

3.3 Catalytic activity in the hydrodeoxygenation of anisole

The catalytic activity of prepared catalysts was evaluated in the hydrodeoxygenation (HDO) of anisole (AN). Reaction conditions in the batch reactor were 280 °C, 7.3 MPa total pressure, and 6 h reaction time. Fig. 11 shows anisole conversions obtained with mono- and bimetallic catalysts. All the catalysts showed activity in this reaction although Pd/S and Pt/S catalysts were less active in anisole conversion than other tested catalysts, which could be due to their low metal content (~1 wt%). According to the activity, the catalysts can be ordered as Pt/S ≈ Pd/S < PdPt/S ≈ Ni/S < NiPt/S < NiPd/S. Anisole conversions obtained at 6 h reaction time with the four most active catalysts (NiPd/S, NiPt/S, PdPt/S and Ni/S) were between 97.1 and 99.0% (Fig. 11, and Table 2). It is worth mentioning that the best activity results were obtained with the bimetallic NiPt/S and NiPd/S catalysts, in which Ni (non-noble metal) was combined with Pt or Pd (noble metals). The above order of activity differs from the order of metal dispersion in the reduced catalysts obtained from the TEM results, where Pd/S catalysts showed the best dispersion (25.0%) followed by NiPt/S (16.4%) and NiPd/S (13.7%). Therefore, not only the dispersion, but also the electronic properties of the bimetallic nanoparticles are important for catalytic performance in HDO.

Fig. 12 shows reaction product compositions obtained in the HDO of anisole with the reduced mono- and bimetallic cat-

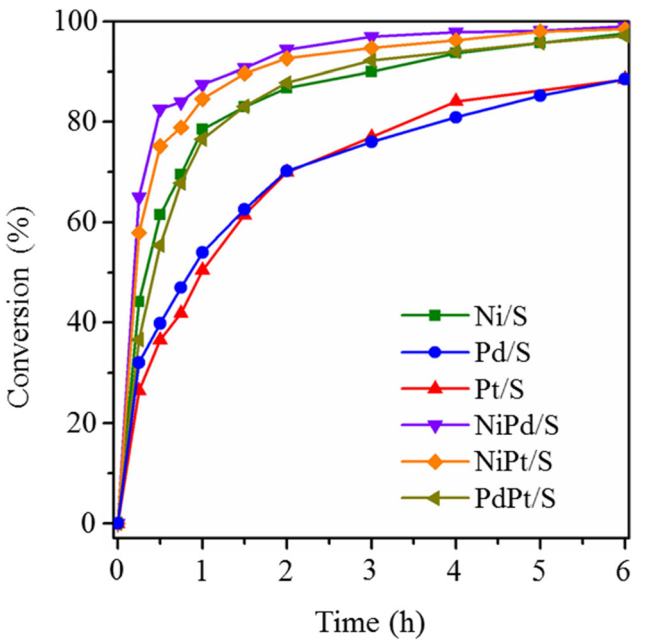

Fig. 11 Conversions of anisole obtained with reduced mono- and bimetallic catalysts. Reaction conditions: batch reactor, 280 °C, 7.3 MPa total pressure.

Table 2 Catalytic performance of the reduced mono- and bimetallic catalysts in the HDO of anisole[a]

Catalyst	Conversion of AN (%)		k_1[b] (h^{-1})	$k_{1N} \times 10^{-4}$ (h^{-1} mol_M^{-1})	k_2[b] (h^{-1})	$k_{2N} \times 10^{-4}$ (h^{-1} mol_M^{-1})	Adj.-R^2	S_{CHA}[c] (%)
	1 h	6 h						
Ni/S	78.5	97.6	1.6	1.8	0.08	0.1	0.96	35.3
Pd/S	53.9	88.6	0.7	6.7	0.04	0.4	0.94	9.3
Pt/S	51.6	88.4	0.6	14.3	0.04	1.0	0.96	9.0
NiPd/S	87.5	99.0	3.2	3.8	0.08	0.1	0.98	38.1
NiPt/S	84.6	98.5	2.5	2.8	0.20	0.2	0.96	71.7
PdPt/S	76.5	97.1	1.4	12.9	0.02	0.2	0.99	5.6

[a] Reaction conditions: batch reactor, 280 °C, 7.3 MPa total pressure. [b] k_1, k_2, pseudo-first-order rate constants for hydrogenation and deoxygenation, respectively, calculated according to the equations $C_{AN} = C_{AN0}\exp(-k_1 \cdot t)$, $C_{CME} = k_1 \cdot C_{AN0}[\exp(-k_1 \cdot t) - \exp(-k_2 \cdot t)]/(k_2 - k_1)$, and $C_{CHA} = C_{AN0} \cdot [1 - \{(k_2\exp(-k_1 \cdot t) - k_1\exp(-k_2 \cdot t)\}/k_2 - k_1)]$. k_{1N} and k_{2N} are pseudo-first-order rate constants normalized per mol of metal (M). [c] Selectivity to cyclohexane at 6 h reaction time defined as % of CHA in the reaction products.

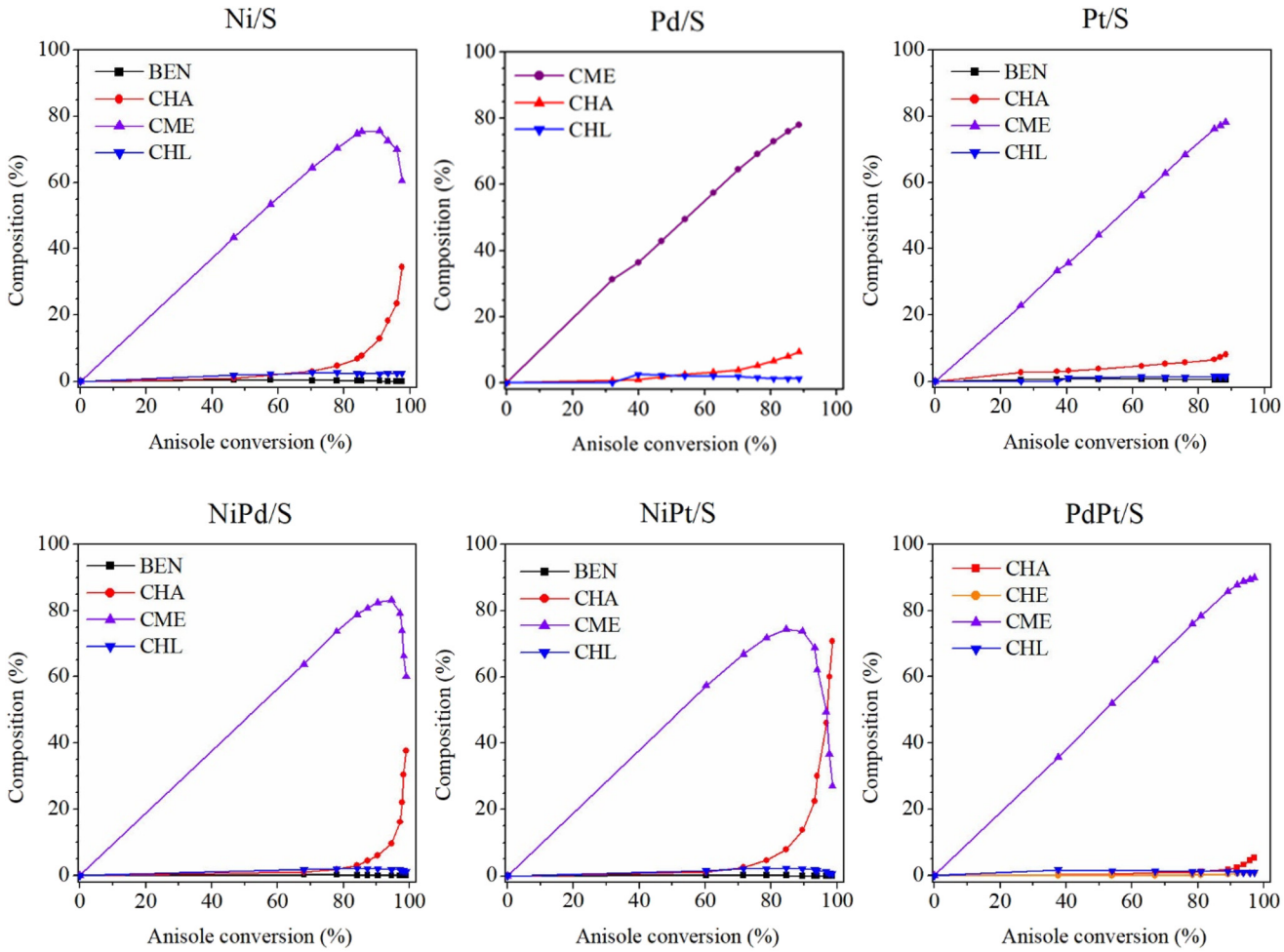

Fig. 12 Reaction product compositions obtained in the HDO of anisole. AN, anisole; CHA, cyclohexane; CHE, cyclohexene; CME, cyclohexyl methyl ether; CHL, cyclohexanol; BEN, benzene.

alysts. The following compounds were identified: cyclohexane (CHA), cyclohexene (CHE), cyclohexyl methyl ether (CME), cyclohexanol (CHL), and benzene (BEN).

According to the observed reaction intermediates, a reaction scheme has been proposed for anisole hydrodeoxygenation over reduced mono- and bimetallic Ni, Pd and Pt catalysts (Scheme 1(A)). For all the catalysts, the main intermediate product was CME, which is formed as a result of hydrogenation of the aromatic ring of anisole over metal nanoparticles. The subsequent cyclohexanol product could be formed

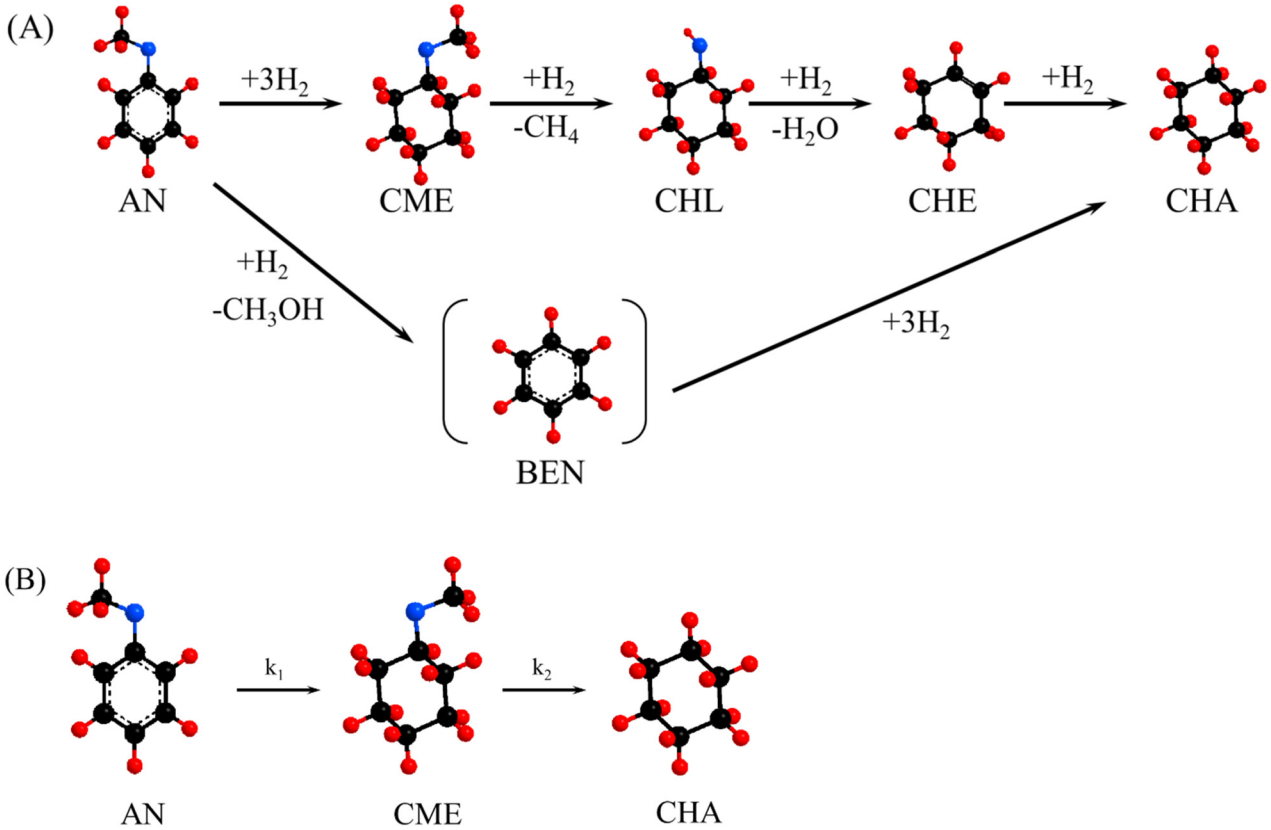

Scheme 1 (A) Proposed reaction mechanism for the hydrodeoxygenation of anisole with prepared mono- and bimetallic catalysts. (B) Simplified reaction mechanism used for the kinetic study. AN, anisole; BEN, benzene; CME, cyclohexyl methyl ether; CHL, cyclohexanol; CHE, cyclohexene and CHA, cyclohexane.

through demethylation of CME. Cyclohexanol, in turn, is subject to dehydration with the formation of cyclohexene, which is quickly hydrogenated giving cyclohexane as the final product. The presence of some traces of BEN suggests the possibility of a second parallel direct deoxygenation reaction route, where anisole is demethylated directly through the hydrogenolysis of $C_{aromatic}$–OCH_3. However, small amounts of obtained BEN (less than 1%) point out that this reaction route is not the main one or that the obtained benzene disappears quickly due to hydrogenation to cyclohexane. Since CME was just one intermediate product formed in considerable amounts during the reaction, it was proposed that the reaction mechanism be simplified, as shown in Scheme 1(B). This simplified reaction mechanism was used for the estimation of the reaction rate constants (k_1 and k_2).

According to previous studies, the predominant route to the HDO of anisole depends on both the acidity of the support and the nature of the metal. The results obtained in the present work with mono- and bimetallic catalysts supported on SBA-15 silica show that, in all cases, the reaction followed the hydrogenation reaction route, which consists of the complete saturation of the aromatic ring of AN before the removal of oxygen. This is reasonable, since metal sites are active for hydrogenation reactions, while the acidic or oxophilic sites play an important role in the hydrogenolysis of the C–O bond. According to Vargas *et al.*,[45] the SBA-15 support has a very small amount of acidic sites, and, therefore, it can be considered that the prepared catalysts have only the metallic active phase (support acidity can be neglected) and both transformations (hydrogenation and hydrogenolysis) take place at the metallic sites. So, metal oxophilicity is important for the formation of deoxygenated products.

Considering the proposed simplified reaction mechanism, shown in Scheme 1(B), and that in catalytic tests hydrogen was always used in large excess with respect to anisole, the reaction rate constants were estimated based on the kinetics of two consecutive pseudo-first-order rate reactions: $AN \xrightarrow{k_1} CME \xrightarrow{k_2} CHA$. The rate constant k_1 represents the hydrogenation of the aromatic ring of AN, while k_2 corresponds to the deoxygenation of the CME intermediate to cyclohexane. Eqn (3)–(5) describe, respectively, the rate of anisole consumption (r_{1AN}) and the rates of formation of cyclohexyl methyl ether (r_{2CME}) and cyclohexane (r_{3CHA}):

$$r_{1AN} = -\frac{dC_{AN}}{dt} = k_1 C_{AN} \quad (3)$$

$$r_{2\,CME} = +\frac{dC_{CME}}{dt} = k_1 C_{AN} - k_2 C_{CME} \quad (4)$$

$$r_{2\,\mathrm{CHA}} = +\frac{\mathrm{d}C_{\mathrm{CHA}}}{\mathrm{d}t} = k_2 C_{\mathrm{CME}} \quad (5)$$

Integrated forms of these equations were used for the rate constant calculations. The system of equations was solved by a non-linear fit of the experimental data. The obtained rate constants are shown in Table 2.

Bimetallic NiPd/S and NiPt/S catalysts showed the highest values of the k_1 rate constants corresponding to the hydrogenation of the AN aromatic ring (3.2 and 2.5 h^{-1}, respectively). Their k_1 values were larger than the sum of k_1 constants of their corresponding monometallic counterparts, pointing out a synergistic effect between both metals (Ni–Pt and Ni–Pd). Interestingly, bimetallic NiPt/S and NiPd/S catalysts and even monometallic Ni/S had higher hydrogenation ability (per gram of the catalyst) than the corresponding only noble metal-containing catalysts (Pd/S, Pt/S and PdPt/S). This can be ascribed to the larger total molar amount of metals in the Ni-containing samples compared to that in the noble metal-containing ones. However, when the k_1 rate constant is normalized per mol of metal in the catalyst (k_{1N}, Table 2), it can be clearly observed that the hydrogenation ability of the monometallic catalysts changes as Ni/S < Pd/S < Pt/S. This order of activity can be expected, since it is well-known that noble metals (NM) are particularly efficient at activating molecular hydrogen, making it capable of reacting with other reactants.[46] For bimetallic catalysts, according to our results, the hydrogenation ability per mol of metal increases in the following order: NiPt/S < NiPd/S < PdPt/S. This order of activity is difficult to predict and it should be related to the dispersion, structure and electronic characteristics of bimetallic nanoparticles.

On the other hand, all the tested catalysts exhibited small values of k_2 and k_{2N}, the reaction rate constants for the deoxygenation of the CME intermediate through $C_{aliphatic}$–O bond cleavage. The highest value of k_2 (0.20 h^{-1}) was obtained for the bimetallic NiPt/S catalyst. Two other Ni-containing catalysts (NiPd/S and Ni/S) showed 2-fold lower k_2 values. Meanwhile, the other tested catalysts (Pt/S, Pd/S and PdPt/S) had a very low hydrogenolysis ability. In this case, it can also be noted that the presence of Ni in the catalysts promotes the C–O bond rupture. Available data in the literature indicate that the oxophilicity of the support, the nature of the supported metal, or a combination of these factors has a great influence on the reaction mechanism in anisole HDO.[47] As the SBA-15 support used in the present work is chemically inert, the ability of the catalysts for O activation should be related to the oxophilic characteristics of the supported metal. The hydrogenating sites provide H, while the oxophilic metal more strongly binds the reactant to the surface through its oxygen functionality, allowing easier C–O scission.[48] According to Kepp,[49] the oxophilicity of the metal is strongly correlated to its electronegativity, since oxygen is highly electronegative. Left-side d-block elements with low effective nuclear charges and electronegativities are thus highly oxophilic. Because of this, Ni has the highest oxophilicity among the studied metals. On resuming analysis of the above catalytic results, it can be concluded that the advantages of the bimetallic NiPd/S and NiPt/S catalysts are due to the combination of highly hydrogenating noble metals such as Pt and Pd and oxophilic Ni species that results in better overall HDO performance. The best selectivity to CHA was obtained with the NiPt/S catalyst (71.7% at 6 h reaction time, Table 2).

Regarding the bimetallic PdPt/S catalyst, it showed a k_1 value (1.4 h^{-1}) only slightly higher than the sum of the k_1 values of the corresponding monometallic Pd/S and Pt/S catalysts (0.7 h^{-1} and 0.6 h^{-1}, respectively, Table 2). This result could be due to the formation of bimetallic Pd–Pt nanoparticles with heterogeneous distribution of metals (Pd-rich and Pt-rich domains, as shown by HAADF-STEM characterization in Fig. 10). The Pd/S and PdPt/S catalysts were the most selective for the formation of the hydrogenated CME intermediate product (about 93% at 6 h reaction time, Fig. 12), which can be useful for the reactions, whose objective is only the hydrogenation of aromatic rings in O-containing reactant molecules.

Finally, the catalytic activity of mono- and bimetallic catalysts supported on the SBA-15 material was compared to that of previously published results for anisole HDO. The values of k_1 of our NiPd/S and NiPt/S catalysts (3.2 and 2.5 h^{-1}) were higher than those reported previously for Ni/SBA-15 catalysts with 4 and 10 wt% Ni (~1.5 h^{-1})[31,45] and Ni/USY, Ru/USY and Pd/USY (all with a 5 wt% metal charge, k_1 between 0.52 and 1.80 h^{-1}).[50] However, the k_2 value of our NiPt/S catalyst was much lower (0.20 h^{-1}) than that of the Ni, Ru and Pd catalysts supported on USY zeolite (2.94 to 9.30 h^{-1}), which could be due to the very low acidity of the SBA-15 silica compared to that of the USY zeolite. It would be interesting to inquire into the HDO behavior of bimetallic NiPt and NiPd catalysts supported on acidic materials instead of on the inert silica support.

4. Conclusions

In this work, bimetallic NiPd, NiPt, and PdPt catalysts supported on SBA-15 silica were synthesized, characterized and their catalytic performance was evaluated in the HDO of anisole. A comparison of different bimetallic catalysts, as well as of bimetallic *vs.* corresponding monometallic analogs, was performed. It was observed that among all the catalysts studied, the bimetallic NiPt/S and NiPd/S catalysts have the best catalytic performance in the HDO of anisole, namely, higher anisole conversions and selectivity to cyclohexane. This was attributed to a combination in these catalysts of noble metal (Pt, Pd) with non-noble more oxophilic Ni metal and to the formation of bimetallic nanoparticles in the reduced catalysts. The main HDO reaction route in all cases was a consecutive reaction through the hydrogenation of the aromatic ring of anisole and then subsequent deoxygenation of the CME intermediate, leading to the final CHA product. Other intermediate products (BEN, CHL and CHE) were formed only in small amounts. Among the two most promising catalysts of NiPd/S

and NiPt/S, the former was found to be slightly better for the hydrogenation of the aromatic ring of anisole, while the latter showed higher deoxygenation ability among all the tested samples, giving ~72% selectivity to cyclohexane at 6 h reaction time. The PdPt/S bimetallic catalyst showed the best selectivity for the formation of the CME intermediate (~93% at 6 h reaction time), which can be useful for the hydrogenation of aromatic rings in O-containing reactants with the formation of saturated O-containing products.

Author contributions

D. P.: writing – original draft, investigation, conceptualization, formal analysis, and visualization. H. V.: investigation and formal analysis. R.M.-C.: investigation, formal analysis, and writing – review & editing. T. K.: writing – review & editing, conceptualization, funding acquisition, and supervision. All authors have given approval to the final version of the manuscript.

Conflicts of interest

There are no conflicts to declare.

Acknowledgements

D. P. acknowledges Consejo Nacional de Humanidades, Ciencias y Tecnologías (CONAHCyT, México) for his Ph. D. scholarship through CVU: (854325). The authors thank X. Bokhimi, A. Morales Espino, C. Salcedo Luna and I. Puente Lee for technical assistance with XRD, SEM and TEM characterization studies. Financial support from Dirección General de Asuntos de Personal Académico – Universidad Nacional Autónoma de México, DGAPA-UNAM, México [grants IN-116324 and IA-106623] is gratefully acknowledged.

References

1 United Nations Environments Programme (2023), Emissions Gap Report 2023: Broken Record - Temperatures Hit New Highs, yet World Fails to Cut Emissions (Again), Nairobi, 2023.
2 H. Shahbeik, A. Shafizadeh, V. K. Gupta, S. S. Lam, H. Rastegari, W. Peng, J. Pan, M. Tabatabaei and M. Aghbashlo, *J. Cleaner Prod.*, 2023, **413**, 137473.
3 Y. Yang, H. Shahbeik, A. Shafizadeh, N. Masoudnia, S. Rafiee, Y. Zhang, J. Pan, M. Tabatabaei and M. Aghbashlo, *Renewable Energy*, 2022, **201**, 70–86.
4 X. Wang, Z. Zhang, Z. Yan, Q. Li and Y. Zhang, *Appl. Catal., A*, 2023, **662**, 119266.
5 B. Chen, R. Rao, M. Cao, C. He, Y. Qian, X. Qiu and X. Ouyang, *Fuel*, 2022, **313**, 123044.
6 A. G. Gayubo, B. Valle, A. T. Aguayo, M. Olazar and J. Bilbao, *J. Chem. Technol. Biotechnol.*, 2010, **85**, 132–144.
7 P. M. Mortensen, J. D. Grunwaldt, P. A. Jensen, K. G. Knudsen and A. D. Jensen, *Appl. Catal., A*, 2011, **407**, 1–19.
8 I. D. Mora-Vergara, L. Hernández Moscoso, E. M. Gaigneaux, S. A. Giraldo and V. G. Baldovino-Medrano, *Catal. Today*, 2018, **302**, 125–135.
9 P. Sun, Z. Wang, C. Li, B. Tang and C. Peng, *Fuel*, 2024, **361**, 130726.
10 M. Chávez-Sifontes and M. Ventura, *Catalysts*, 2024, **14**(2), 146–168.
11 S. Jin, Z. Xiao, C. Li, X. Chen, L. Wang, J. Xing, W. Li and C. Liang, *Catal. Today*, 2014, **234**, 125–132.
12 L. Wang, C. Li, S. Jin, W. Li and C. Liang, *Catal. Lett.*, 2014, **144**, 809–816.
13 E. Aliu, A. Hart and J. Wood, *Catal. Today*, 2021, **379**, 70–79.
14 E. A. Roldugina, E. R. Naranov, A. L. Maximov and E. A. Karakhanov, *Appl. Catal., A*, 2018, **553**, 24–35.
15 A. S. Ouedraogo and P. R. Bhoi, *J. Cleaner Prod.*, 2020, **253**, 119957.
16 Y. Zhai, M. Chu, N. Shang, C. Wang, H. Wang and Y. Gao, *Appl. Surf. Sci.*, 2020, **506**, 144681.
17 W. Jin, J. Gandara-Loe, L. Pastor-Pérez, J. J. Villora-Picó, A. Sepúlveda-Escribano, R. Rinaldi and T. R. Reina, *Renewable Energy*, 2023, **215**, 118907.
18 I. Faturachman, H. H. Kurniawan, R. T. Yunarti, R. R. Widjaya, A. A. Dwiatmoko, Y. Maryati and N. Rinaldi, *Can. J. Chem.*, 2022, **100**, 583–588.
19 D. Zhao, Q. Huo, J. Feng, B. F. Chmelka and G. D. Stucky, *J. Am. Chem. Soc.*, 1998, **120**, 6024–6036.
20 K. S. W. Sing, D. H. Everett, R. A. W. Haul, L. Moscou, R. A. Pierotti, J. Rouquerol and T. Siemieniewska, *Pure Appl. Chem.*, 1985, **57**, 603–619.
21 Y. Yin, Z. F. Yang, Z. H. Wen, A. H. Yuan, X. Q. Liu, Z. Z. Zhang and H. Zhou, *Sci. Rep.*, 2017, **7**, 4509.
22 D. Ballesteros-Plata, A. Infantes-Molina and E. Rodríguez-Castellón, *Appl. Catal., A*, 2019, **580**, 93–101.
23 H. A. Khan, M. Abou-Daher, A.-L. S. de Freitas, J. Subburaj, O. E. Tall and A. Farooq, *Catal. Today*, 2024, **426**, 114370.
24 P. Sudhakar and A. Pandurangan, *J. Porous Mater.*, 2018, **25**, 747–759.
25 B. H. Chen, Z. S. Chao, H. He, C. Huang, Y. J. Liu, W. J. Yi, X. L. Wei and J. F. An, *Dalton Trans.*, 2016, **45**, 2720–2739.
26 S. Pinchujit, A. Phuruangrat, S. Wannapop, T. Sakhon, B. Kuntalue, T. Thongtem and S. Thongtem, *Solid State Sci.*, 2022, **134**, 107064.
27 J. Liu, G. Xu, Q. An, Y. Wang, Y. Yu and H. He, *ACS Omega*, 2023, **8**, 13944–13954.
28 J. Bassil, A. AlBarazi, P. Da Costa and M. Boutros, *Catal. Today*, 2011, **176**, 36–40.
29 C. Li, Q. Zhang, Y. Wang and H. Wan, *Catal. Lett.*, 2008, **120**, 126–136.
30 M. Boutros, M. E. Gálvez, T. Onfroy and P. Da Costa, *Microporous Mesoporous Mater.*, 2014, **183**, 1–8.

31 L. A. Calzada, D. Pérez-Estrada, M. Sánchez-Ramírez, D. Gómora-Herrera, A. Gómez-Cortés, G. Díaz and T. E. Klimova, *ACS Omega*, 2023, **8**, 42849–42866.
32 M. Pudukudy, Z. Yaakob and Z. S. Akmal, *Appl. Surf. Sci.*, 2015, **353**, 127–136.
33 H. L. Tidahy, M. Hosseni, S. Siffert, R. Cousin, J.-F. Lamonier, A. Aboukaïs, B.-L. Su, J.-M. Giraudon and G. Leclercq, *Catal. Today*, 2008, **137**, 335–339.
34 L. Guo, Y. Tian, X. He, C. Qiao and G. Liu, *Fuel*, 2022, **322**, 124082.
35 W. Hume-Rothery, R. E. Smallman and C. W. Haworth, *The Structure of Metals and Alloys*, Metals & Merallurgy Trust, London, 1969.
36 A. Christensen, A. Ruban, P. Stoltze, K. Jacobsen, H. Skriver, J. Nørskov and F. Besenbacher, *Phys. Rev. B: Condens. Matter Mater. Phys.*, 1997, **56**, 5822–5834.
37 G. Guisbiers, R. Mendoza-Pérez, L. Bazán-Díaz, R. Mendoza-Cruz, J. Jesús Velázquez-Salazar and M. José-Yacamán, *J. Phys. Chem. C*, 2017, **121**, 6930–6939.
38 K. Persson, A. Ersson, S. Colussi, A. Trovarelli and S. G. Järås, *Appl. Catal., B*, 2006, **66**, 175–185.
39 P. Qu, S. Wang, W. Hu, Y. Wu, J. Chen, G. Zhang, P. Shen, Y. Chen and L. Zhong, *Catal. Commun.*, 2020, **135**, 105900.
40 X. Meng, M. Bi and W. Gao, *Sens. Actuators, B*, 2023, **390**, 133976.
41 J. Escobar, J. A. Colín-Luna and M. C. Barrera, *Ind. Eng. Chem. Res.*, 2024, **63**, 1248–1260.
42 C. A. Teles, C. Ciotonea, N. Gomes, V. O. O. Gonçalves, A. Ungureanu, C. Catrinescu, M. Marinova, J.-M. Clacens, S. Royer, F. B. Noronha and F. Richard, *Appl. Catal., A*, 2022, **641**, 118686.
43 A. Borodzinski and M. Bonarowska, *Langmuir*, 1997, **13**, 5613–5620.
44 G. Guisbiers, R. Mendoza-Cruz, L. Bazán-Díaz, J. J. Velázquez-Salazar, R. Mendoza-Perez, J. A. Robledo-Torres, J.-L. Rodriguez-Lopez, J. M. Montejano-Carrizales, R. L. Whetten and M. José-Yacamán, *ACS Nano*, 2016, **10**, 188–198.
45 H. Vargas-Villagrán, M. A. Flores-Villeda, I. Puente-Lee, D. A. Solís-Casados, A. Gómez-Cortés, G. Díaz-Guerrero and T. E. Klimova, *Catal. Today*, 2020, **349**, 26–41.
46 Z. He and X. Wang, *Catal. Sustainable Energy*, 2013, **1**, 28–52.
47 Q. Tan, G. Wang, A. Long, A. Dinse, C. Buda, J. Shabaker and D. E. Resasco, *J. Catal.*, 2017, **347**, 102–115.
48 A. M. Robinson, J. E. Hensley and J. W. Medlin, *ACS Catal.*, 2016, **6**, 5026–5043.
49 K. P. Kepp, *Inorg. Chem.*, 2016, **55**, 9461–9470.
50 D. P. Gamliel, S. Karakalos and J. A. Valla, *Appl. Catal., A*, 2018, **559**, 20–29.